

ARTICLE

DOI: 10.1038/s41467-018-03652-8

OPEN

The ng ζ 1 toxin of the gonococcal epsilon/zeta toxin/antitoxin system drains precursors for cell wall synthesis

Andrea Rocker¹, Madeleine Peschke¹, Tiia Kittilä¹, Roman Sakson¹, Clara Brieke¹ & Anton Meinhart^{1,2}

Bacterial toxin–antitoxin complexes are emerging as key players modulating bacterial physiology as activation of toxins induces stasis or programmed cell death by interference with vital cellular processes. Zeta toxins, which are prevalent in many bacterial genomes, were shown to interfere with cell wall formation by perturbing peptidoglycan synthesis in Gram-positive bacteria. Here, we characterize the epsilon/zeta toxin–antitoxin (TA) homologue from the Gram-negative pathogen *Neisseria gonorrhoeae* termed ng ϵ 1 / ng ζ 1. Contrary to previously studied streptococcal epsilon/zeta TA systems, ng ϵ 1 has an epsilon-unrelated fold and ng ζ 1 displays broader substrate specificity and phosphorylates multiple UDP-activated sugars that are precursors of peptidoglycan and lipopolysaccharide synthesis. Moreover, the phosphorylation site is different from the streptococcal zeta toxins, resulting in a different interference with cell wall synthesis. This difference most likely reflects adaptation to the individual cell wall composition of Gram-negative and Gram-positive organisms but also the distinct involvement of cell wall components in virulence.

¹Department of Biomolecular Mechanisms, Max Planck Institute for Medical Research, Jahnstr. 29, 69120 Heidelberg, Germany. ²Present address: Research Institute for Molecular Pathology (IMP), Vienna Biocenter (VBC), Campus-Vienna-Biocenter 1, 1030 Vienna, Austria. These authors contributed equally: Andrea Rocker, Madeleine Peschke. Correspondence and requests for materials should be addressed to A.M. (email: Anton.Meinhart@imp.ac.at)

Bacterial toxin–antitoxin (TA) modules are poisonous gene pairs coding for a toxin and its cognate antitoxin. TA systems are highly prevalent in bacterial genomes^{1,2} and in most cases the neutralizing antitoxin is encoded together with the toxin on a bicistronic locus^{3,4}. TA modules were initially discovered as plasmid stabilizing systems, but have since been shown to regulate persister cell and biofilm formation, to act as stress response elements and even to increase virulence of pathogenic bacteria^{5–7}. Because of their roles in bacterial survival, TA systems have become interesting targets for the development of new antimicrobial agents. Detailed understanding of TA systems is, however, required before such approaches can be efficiently utilized.

TA modules can be grouped into six different types varying in their mode of toxin inhibition⁸. Typically, the toxin is a protein whereas the antitoxin can be either a protein or a non-coding RNA. The best characterized family of TA systems are the type II systems where both the toxin and the antitoxin are proteins^{3,9}. Neutralization of the toxin is achieved in type II systems through complex formation between the two proteins. Regardless of the TA system type, toxins interfere with vital cellular pathways leading to cell death or dormancy¹⁰. Most toxins known to date target protein translation, e.g., by cleavage of mRNAs^{11–13}, modification of tRNAs,^{14,15} or inhibition of ribosome activity¹⁶. However, toxins have also been shown to inhibit replication

and to prevent ATP synthesis by pore formation^{19,20}. In addition, one group of type II toxins, the so called zeta toxins, interfere with cell wall integrity by phosphorylating cytosolic cell wall precursors²¹ and are highly prevalent in pathogenic bacteria²².

Zeta toxins are canonical type II TA systems in which the toxicity of zeta is inhibited by the epsilon antitoxin. The first characterized members of this family were the plasmid encoded ϵ/ζ from *Streptococcus pyogenes*²³ and the chromosomally encoded PezAT systems from *Streptococcus pneumoniae*²⁴. Zeta toxins adopt a classical phosphotransferase fold^{24,25} with a central P-loop motif important for ATP binding²⁶. In contrast, the cognate epsilon antitoxin folds into a simple three helix bundle domain. Both streptococcal systems form an $\epsilon_2\zeta_2$ heterotetramer, in which the ATP binding to the active site of zeta is blocked by epsilon impairing zeta activity. In fact, zeta toxins use ATP to phosphorylate UDP-*N*-acetylglucosamine (UNAG) to form UDP-*N*-acetylglucosamine-3'-phosphate (UNAG-3P)²¹ and thereby modify this essential peptidoglycan precursor. Biosynthesis of peptidoglycan is highly conserved in bacteria and requires a cascade of enzymes that sequentially modify UNAG²⁷. Initially, an enolpyruvate group is added to the C3'-OH group of UNAG by MurA yielding UDP-acetylglucosamine enolpyruvate (EP-UNAG). Because zeta toxins and MurA act on the same C3'-OH group, formation of UNAG-3P inhibits formation of EP-UNAG. When zeta is inactive, e.g., by binding to the epsilon antitoxin, the

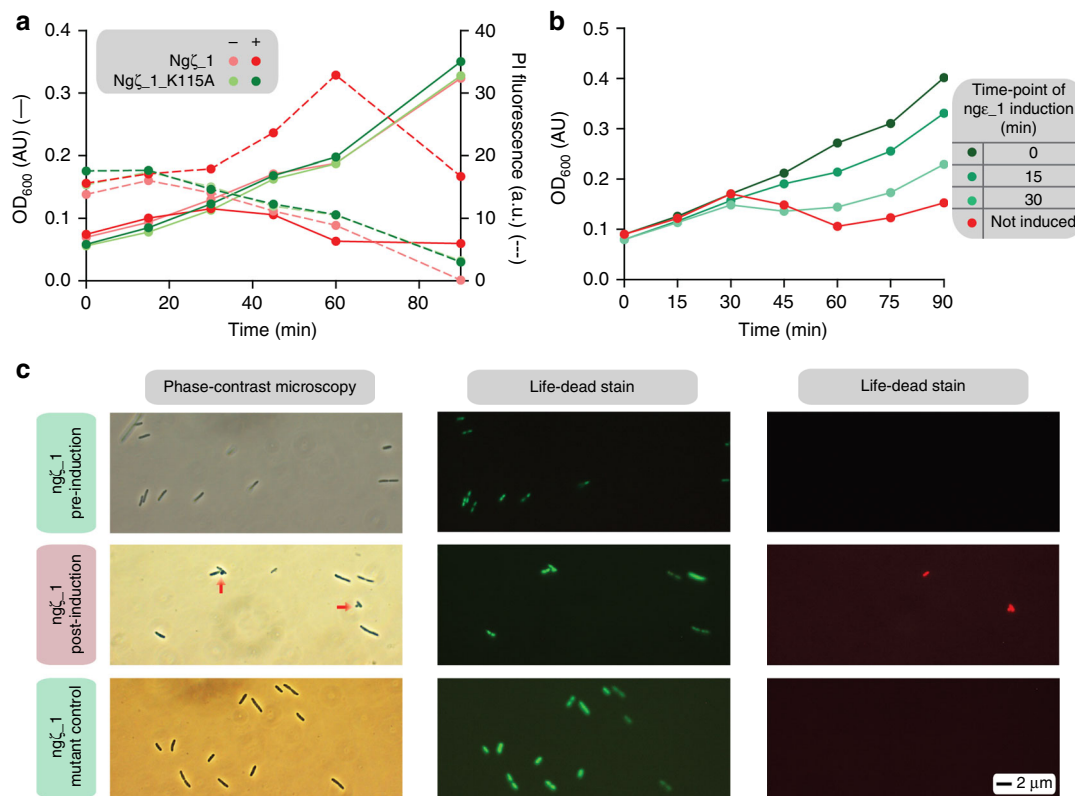


Fig. 1 Ng ζ _1 expression in *E. coli* cells causes a lytic phenotype compensated by *nge_1* co-expression. **a** Growth curves of *E. coli* C41(DE3) cells expressing ng ζ _1 (red solid line and left Y-axis) or ng ζ _1(K115A) (forest-green solid line and left Y-axis) together with the corresponding propidium iodide influx into the cells (dashed lines similarly colored and right Y-axis). Control experiments in which expression of ng ζ _1 or ng ζ _1(K115A) was not induced are shown in light pink and lime-green. Note that growth curves of the two uninduced cell cultures as well as the PI measurements of the mutated variant (induced and not induced) fully overlay with each other. **b** Growth curves of *E. coli* BL21(DE3)-RIL cells co-expressing ng ζ _1 and *nge_1*. Expression of *nge_1* was induced 0 (forest-green), 15 (lime-green) and 30 min (pale-green) subsequent to ng ζ _1 induction. The control experiment in which expression of *nge_1* was not induced is shown in red. **c** Phase contrast and fluorescence microscopy (live-dead stain) of *E. coli* C41(DE3) cells before and after ng ζ _1 induction (30 min) and the control experiment using the inactive ng ζ _1(K115A) mutant. Cells with green fluorescence have intact cell membranes and are alive. Membrane permeable cells have red fluorescence due to propidium iodide influx. Resolved bulges due to cell wall extrusions in phase-contrast microscopy images are highlighted with red arrows

enolpyruvate moiety of EP-UNAG is reduced by MurB yielding UDP-muramic acid (UNAM), the activated sugar to which a peptide stem is attached. Importantly, UNAG-3P is not only a dead-end product of zeta toxins but acts as a potent inhibitor of MurA²¹. Eventually, the combined types of MurA inhibition stall de novo peptidoglycan synthesis at this early step and thus cause cell lysis in rapidly dividing bacteria.

Only epsilon/zeta modules of Gram-positive bacteria have been characterized so far in detail, but homologs are also highly prevalent in Gram-negative bacteria²². In contrast to zeta toxins from Gram-positive prokaryotes, the few investigated homologous TA systems of Gram-negative bacteria seem to be much more diverse in their function and mechanisms. For instance, the structurally homologous plant effector protein AvrRxo1 from *Xanthomonas*²⁸ functions as a bacterial TA-system as well²⁹. AvrRxo1 has been shown to phosphorylate NAD and its precursors NAAD in vitro and causes massive 3'-NADP accumulation in vivo^{30,31}. On the other side, a zeta homologue that is prevalent in *Escherichia coli* strains combines toxin and antitoxin functionalities in a single polypeptide chain³².

A prototype of a Gram-negative epsilon/zeta TA module, the epsilon_1/zeta_1 (*nge_1/ngz_1*) TA system, is encoded by *Neisseria gonorrhoeae*, an obligate human pathogen causing the sexually transmitted disease gonorrhoea³³. Traditional antibiotic treatment of gonorrhoea consists of ampicillin and tetracycline but this therapy is threatened by the spread of antibiotic resistances. High-level tetracycline resistance is conferred by the *tetM* determinant of 25.2 MDa conjugative plasmids and can thereby rapidly spread across the population³⁴. The *tetM* determinant was acquired by insertion into the genetic load region of smaller 24.5 MDa conjugative plasmids of the “Dutch” or “American” type³³. Sequence analysis of the *tetM*-less ancestor as well as different 25.2 MDa plasmids revealed the presence of the *nge_1/ngz_1* locus in all plasmids³³. Interestingly, all three different conjugative plasmids were shown to contain a second epsilon/zeta homologous locus that has diverged by extensive mutations between the 25.2 MDa *tetM*-containing and the 24.5 MDa conjugative plasmids. *TetM*-containing plasmids carry the epsilon_2/zeta_2 locus, 24.5 MDa conjugative plasmids carry the epsilon_3/zeta_3 locus³³. Whereas the diverged epsilon_2/zeta_2 and epsilon_3/zeta_3 TA systems seem to be very similar in their amino acid sequence to the well characterized streptococcal systems (around 40% amino acid sequence homology), *nge_1/ngz_1* seems to be very different even at this level. However, nothing is known about these two gene pairs and therefore the mechanistic relevance of two homologous systems on the same plasmid remained unclear so far. Thus, we set out to investigate the *nge_1/ngz_1* locus of *N. gonorrhoeae*. We could show that *ngz_1*, like streptococcal zeta toxins, phosphorylates peptidoglycan precursors and efficiently inhibits cell wall synthesis. However, in contrast to the known zeta toxins, *ngz_1* showed topological rewiring and a hitherto unknown enzymatic activity by phosphorylating UDP-activated sugars at the C4'-OH group of the hexose moiety. This phosphorylation led to formation of dead-end metabolites resulting in cell death by draining precursors required for cell wall synthesis. As phosphorylation of the C4'-OH group has not been observed for the previously characterized epsilon/zeta systems, *ngz_1* and its proteobacterial homologs form a yet undescribed subfamily of zeta toxins.

Results

***ngz_1* forms a new subclass of zeta-like toxins.** Bioinformatic analysis of *nge_1/ngz_1* revealed *ngz_1* toxins to be prevalent in numerous *N. gonorrhoeae* isolates (with currently 46 different NCBI entries with 100% sequence identity) but also a significant

number of closely related zeta homologs in more than 25 different, mainly pathogenic proteobacteria was found (Supplementary Fig. 1 and Supplementary Table 1). However, apart from being encoded on a bicistronic operon³³ and harbouring a P-loop motive, a hallmark for ATP/GTP binding proteins²⁶, *ngz_1* is remarkably different from the hitherto functionally characterized streptococcal zeta toxins^{21,35} in its primary sequence. Especially striking is that the P-loop motive is located much closer to the C-terminus when compared with streptococcal zeta toxins (Supplementary Fig. 1). Furthermore, also the *nge_1* antitoxin has no similarities to any known epsilon protein. Thus, we first questioned, whether *nge_1/ngz_1* is a functional TA system at all.

When *ngz_1* was expressed in *E. coli* cells, we observed a strong lytic phenotype 30 min post-induction as monitored by a decrease in optical density at 600 nm (OD₆₀₀) paired with an influx of propidium iodide (Fig. 1a). This toxic phenotype was suppressed

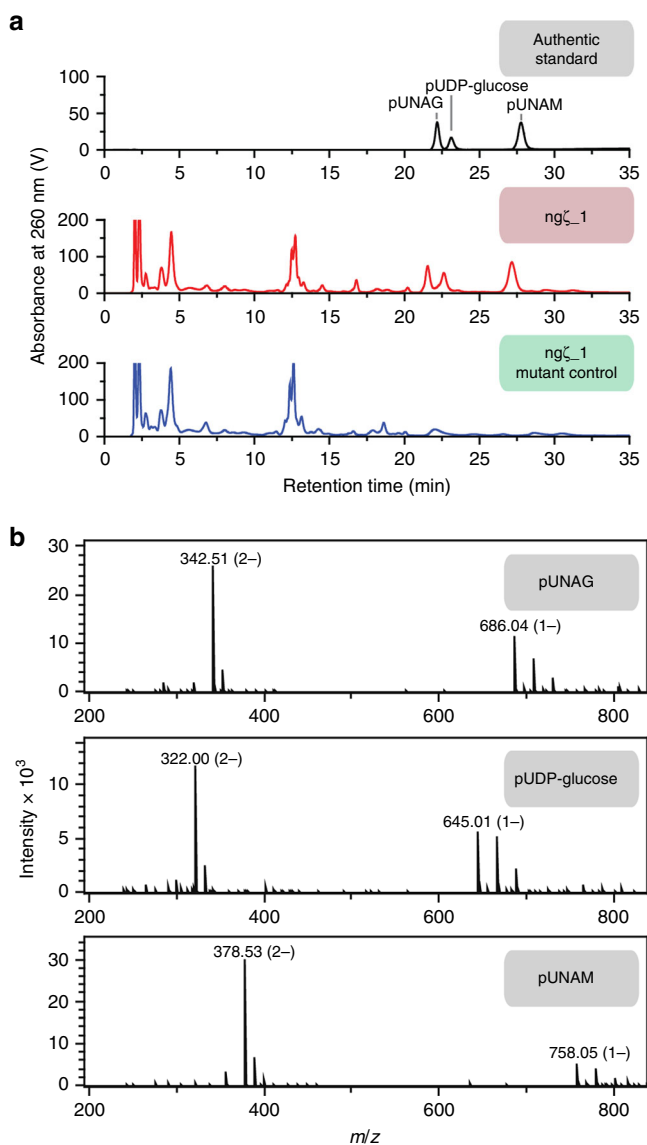


Fig. 2 *Ngz_1* phosphorylates different UDP-activated sugar species. **a** High pressure liquid chromatography analysis of small metabolite extracts from *E. coli* strain C41(DE3) cells expressing either *ngz_1* (red) or the inactive *ngz_1*(K115A) variant (blue). Separation of UNAG, UDP-glucose and UNAM phosphorylated by *ngz_1* in vitro are shown for genuine standards (gray). **b** Mass determination of isolated, phosphorylated UNAG, UDP-glucose and UNAM by ESI-MS

when nge_1 was simultaneously expressed in *trans* (Fig. 1b) indicating that nge_1 and ngz_1 together are indeed a TA pair. However, induction of nge_1 15 or 30 min after ngz_1 was not sufficient to inhibit the lytic phenotype completely (Fig. 1b). Similar as reported for the pneumococcal zeta toxin²⁴, cell growth resumed in those experiments approximately 60 min after induction in all cases (Fig. 1b). Live/dead staining showed propidium iodide influx after induction of ngz_1 and substantial cell wall defects of ngz_1 expressing cells were observed (Fig. 1c). In order to provide evidence that a potential kinase activity of ngz_1 causes the lytic phenotype, the catalytic lysine residue in the P-loop was altered to alanine (ngz_1(K115A)). Cells expressing this variant grew similar to cells co-expressing ngz_1 and nge_1 (Fig. 1a, c). In conclusion, these findings strongly suggest that nge_1/ngz_1 is indeed an authentic TA operon and that the toxic effect of ngz_1 is caused by its kinase activity.

ngz_1 phosphorylates peptidoglycan precursors. We wondered whether similar to the streptococcal zeta toxins²¹ ngz_1 also phosphorylates UNAG. Thus, we isolated small metabolite extracts from cells expressing ngz_1 or the catalytically inactive variant and separated these extracts by high performance liquid chromatography (HPLC) (Fig. 2a). Surprisingly, we observed significant accumulation of three new species exclusively in ngz_1-poisoned cell extracts, a finding which sets ngz_1 apart from the hitherto characterized zeta toxins that only showed UNAG-3P enrichment²¹. These three species were isolated and their masses were determined by ESI-MS (Fig. 2b). The eluting species had a molecular mass comparable to that of a phosphorylated, deprotonated modification of UNAG ($m_{\text{obs.}} = 686.04$ Da; $m_{\text{calc.}} = 686.04$ Da; first eluting species), of UDP-glucose/UDP-galactose ($m_{\text{obs.}} = 645.01$ Da; $m_{\text{calc.}} = 645.12$ Da; second eluting species), and of UNAM ($m_{\text{obs.}} = 758.05$ Da; $m_{\text{calc.}} = 758.39$ Da, third eluting species). The second species is most likely phosphorylated UDP-glucose and not UDP-galactose since the *E. coli* strain C41(DE3) used in the experiment lacks the *galT* and *galE* genes^{36,37} and is thus defective in UDP-galactose synthesis³⁸. Detecting phosphorylated UNAM was quite surprising as the hitherto characterized zeta toxins phosphorylate UNAG at C3'-OH group²¹, which is blocked by a lactoyl group in case of UNAM (Supplementary Fig. 2). These results strongly suggest that ngz_1 phosphorylates UDP-sugars at a different site when compared with previously characterized zeta toxins.

To further verify the identity of these products, we tested the *in vitro* activity of ngz_1, which was separated from nge_1 chromatographically (Supplementary Fig. 3), for different UDP-sugars. In a coupled spectroscopic assay, UNAM strongly stimulated ATPase activity of the protein, but we could not detect significant amounts of ADP production when either UNAG or UDP-glucose were added (Supplementary Fig. 4a).

To account for low reaction rates, we incubated ngz_1 with UDP-glucose (Supplementary Fig. 4b) or UNAG (Supplementary Fig. 4c) for up to 24 h and analysed the products by anion exchange chromatography. Indeed, phosphorylated products were detected in all cases. However, ADP production was found to be in excess over formation of phosphorylated UNAG when monitoring ngz_1 activity over long periods of time. Surprisingly, the phosphorylated species vanished, when the assay was incubated for 12 h (Supplementary Fig. 4c) indicating a phosphatase activity of either ngz_1 or an unidentified contamination. Ultimately, the three phosphorylated *in vitro* products were isolated and analysed by HPLC, where they had the same retention times as the species formed *in vivo* (Fig. 2a). Altogether, these results show, that ngz_1 phosphorylates several

Table 1 Data collection and refinement statistics

	nge_1/ngz_1 (K115A) Se- Met	nge_1/ngz_1 UNAM	nge_1/ngz_1 UNAM-4P
Data collection			
Space group	$P 2_1$	$P 2_1$	$P 2_1$
Cell dimensions			
<i>a</i> , <i>b</i> , <i>c</i> (Å)	79.8, 149.6, 125.1	80.3, 148.2, 124.4	80.5, 149.3, 125.4
α , β , γ (°)	90, 94.82, 90	90, 93.88, 90	90, 94.35, 90
Resolution (Å)	50-2.4 (2.8-2.4)	50-2.7 (2.8-2.7)	50-2.8 (2.9-2.8)
$R_{\text{meas.}}$	21.5 (152.2)	9.7 (99.1)	11.3 (92.0)
$I/\sigma I$	11.8 (2.5)	12.0 (1.7)	11.3 (1.9)
Completeness (%)	99.7 (99.6)	99.4 (99.2)	98.6 (89.6)
Redundancy	13.9 (13.7)	4.2 (4.1)	4.1 (3.8)
CC _{1/2}	99.8 (82.6)	99.4 (70.4)	99.7 (74.4)
Refinement			
Resolution (Å)	50-2.4	50-2.7	50-2.8
No. reflections	108,038	75,069	68,024
$R_{\text{work}}/R_{\text{free}}$	22.9 / 26.9	22.1 / 24.6	21.9 / 24.4
No. atoms			
Protein	14,071	14,039	14,055
Ligand/ion	110	262	275
Water	110	104	141
B -factor			
Protein	51.6	68.0	62.5
Ligand/ion	65.3	68.4	55.4
Water	40.8	48.8	42.8
R.m.s. deviations			
Bond lengths (Å)	0.011	0.008	0.007
Bond angles (°)	1.38	1.17	1.13
Atomic coordinates	6EPG	6EPH	6EPI

peptidoglycan precursors and most likely does so at a site different from the streptococcal zeta toxins.

Architecture of the nge_1/ngz_1 TA-complex. In order to gain detailed insights into the zeta toxin encoded by *Neisseria gonorrhoeae*, we aimed at a structural characterization of substrate and product bound states of ngz_1. To this end, we first determined the crystal structure of the catalytically inactive nge_1/ngz_1 (K115A) selenomethionine substituted protein complex at 2.4 Å resolution using single anomalous dispersion experiments (Table 1). We found four heterodimeric nge_1/ngz_1 (K115A) TA complex molecules located in the asymmetric unit, a complex arrangement which we also observed in solution (Supplementary Fig. 5). Thus, the quaternary structure of the observed heterodimeric nge_1/ngz_1 protein complex is substantially different to the hitherto described heterotetrameric oligomeric state for all other epsilon/zeta TA complexes^{24,25}.

In fact, not only the quaternary structure is set apart from known zeta toxins, but also the tertiary structure and mode of inhibition is very different to other zeta toxins. Strikingly nge_1 binds as an extended polypeptide stretch onto the molecular surface of ngz_1 and does not fold into a globular domain (Fig. 3a, b). In contrast, the streptococcal epsilon antitoxins fold into three-helix bundles (Supplementary Fig. 6) and two epsilon molecules form the core of the heterotetrameric epsilon₂/zeta₂ protein complex^{24,25}. Furthermore, the C-terminal part of the first helix, the second helix and the connecting loop region of

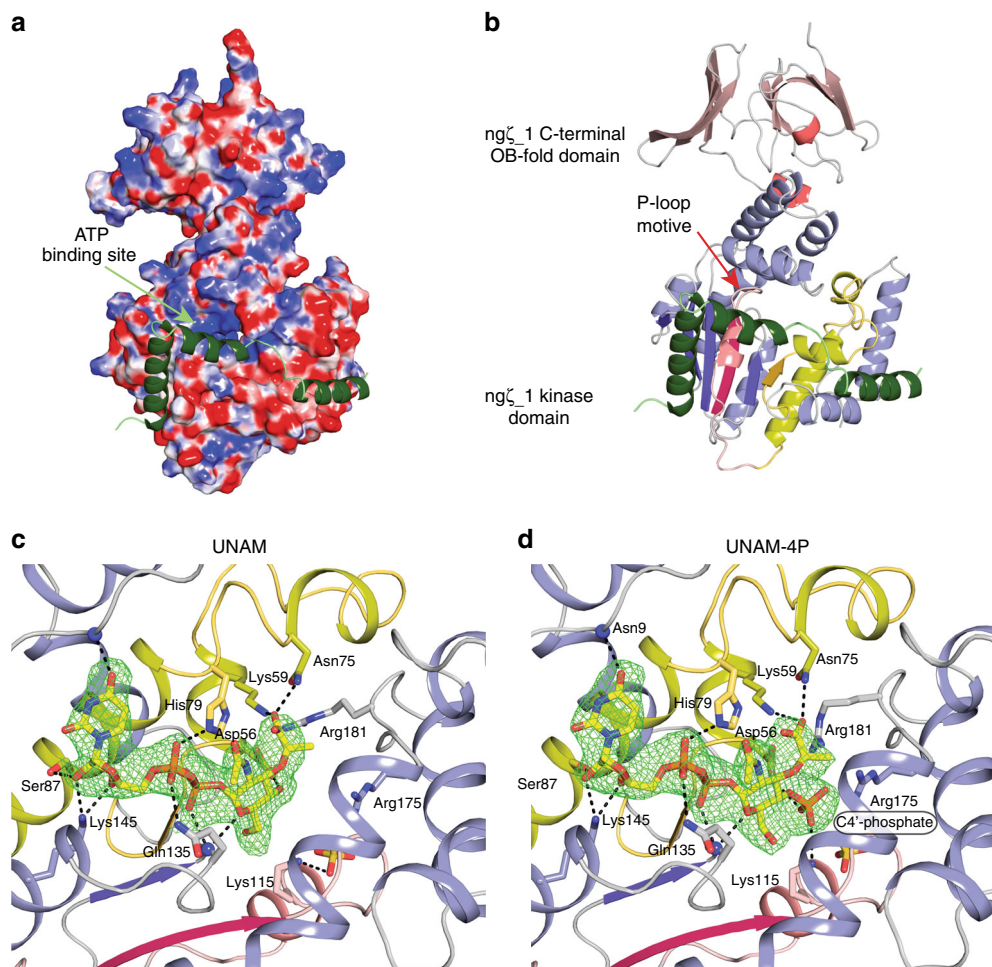


Fig. 3 Structure of the *nge_1/ngz_1* TA complex and substrate binding mode. **a** Surface representation of *ngz_1* colored according to the electrostatic surface-potential and *nge_1* depicted as ribbon model (forest-green). **b** Ribbon representation of *ngz_1* at the same orientation as in **a**. Structural elements involved in topological rewiring are highlighted in red (strand)/pink (helix) and dark-yellow (strand)/yellow (helix). The C-terminal OB-fold domain is colored in red. Coloring is performed similar as in Supplementary Fig. 1. **c, d** Close-up view of the active site of *ngz_1* with the bound UNAM (**c**) and UNAM-4P (**d**) molecules shown as stick model. Fo-Fc electron density map contoured at 3σ with the ligand omitted before refinement is shown as a mesh

nge_1 cover the potential ATP binding site (Fig. 3a). In all other epsilon toxins, residues located in the N-terminal region of the first helix of the three-helix bundle protrude into the active site and block ATP binding to the toxic kinase domain^{24,25}.

In addition, also the tertiary structure of *ngz_1* is different to known zeta toxins, as it consists of two domains (Fig. 3b). The N-terminal domain has the classical fold of a nucleotide kinase to which a DALI search³⁹ identified zeta toxins^{24,25} and AvrRxo1 from *Xanthomonas*²⁸ to be the closest structural homologues. Although our initial analysis of the primary sequence did not identify these homologues, a structural alignment revealed that two sequence blocks were shuffled by swapping position within the polypeptide chain. Yet, two loop regions were topologically rewired in *ngz_1* when compared with other zeta toxins leading to a similar tertiary structure albeit these two blocks occur at different position within the amino acid sequence (Supplementary Fig. 1). Nevertheless, residues that have previously been shown to be important for enzyme catalysis are found to be structurally conserved in *ngz_1*. Finally, the C-terminal domain has the fold of an oligonucleotide/oligosaccharide binding domain (OB-domain) and consists of a five-stranded Greek-key β -barrel that is in an open distorted conformation capped by a short α -helix. Although found in all gonococcal zeta toxins, only the zeta homologue of *Eikenella sp. NML01-A-086* contained a similar domain.

***ngz_1* phosphorylates UNAM at the 4'-hydroxy group.** Since we found UNAM to be a superb substrate in vitro compared to all other candidates which we identified by small metabolite extracts, we soaked UNAM into crystals and determined the structure of the complex. Indeed we observed a strong electron density for a UNAM molecule positioned in the active site of all four *ngz_1* polypeptide chains (Fig. 3c). To our surprise, Asp56, which most likely deprotonates the substrate before nucleophilic attack on the γ -phosphate group, is in hydrogen bonding distance to the C4'-OH group of the hexose moiety of UNAM, substantiating phosphorylation of this particular group. Indeed, by soaking purified, *ngz_1* phosphorylated UNAM into our crystals we unambiguously showed that the phosphate group on UNAM was attached to the C4'-OH (Fig. 3d) and not to the C3'-OH group atom, different to what has been described for the hitherto characterized zeta UNAG kinases²¹. We observed a number of interactions between *ngz_1* and UNAM (Fig. 3c, d) and nearly all residues that form hydrogen bonds with UNAM are strictly conserved among homologues, but not in authentic UNAG-3' kinases (Supplementary Fig. 1). Most importantly, Asn75 and Lys59 form hydrogen bonds with the 1-carboxyethyl group of UNAM which could explain the preference of UNAM over UNAG by *ngz_1*. Moreover, Arg181 and Arg175 form a positively charged patch in the active site counteracting the negatively

charged phosphate groups. When comparing the configuration of UNAM bound to *ngz_1* with UNAG bound to *S. pyogenes* zeta toxin²¹, we found a UDP-sugar binding mode to the active site that follows a rigid-body rotation by 180° (Supplementary Fig. 7), causing that the C4'-OH and not the C3'-OH group is located in close proximity to the catalytic important aspartic acid (Asp56 in *ngz_1* and Asp67 in *S. pyogenes* zeta toxin). To exclude that UNAG could be phosphorylated at a different site than UNAM we verified the specificity of *ngz_1* towards the less preferred UNAG and confirmed phosphorylation of the C4'-OH group of the *N*-acetylglucosamine moiety by nuclear magnetic resonance (NMR) (Supplementary Fig. 8). In fact, no evidence accumulated from our NMR experiments that indicated any phosphorylation event other than that occurring at the C4'-OH. Similarly, exclusive C3'-OH phosphorylation was shown for streptococcal zeta toxins²¹. Thus, no promiscuity towards the phosphorylation site is given and the observed phosphorylation event is not a side reaction in either case. In conclusion, *ngz_1* performs a yet undescribed phosphorylation of the C4'-OH groups of UDP-sugars.

A non-discriminative blockade drains peptidoglycan synthesis.

Our small metabolite extracts demonstrated no significant difference in the concentration of the three accumulating, phosphorylated UDP-sugars (Fig. 2a). Yet, our initial qualitative in vitro activity assays pointed to an increased activity of *ngz_1* for UNAM (Supplementary Fig. 4a). Thus, we wondered which factors determine to which extent each individual *ngz_1* product accumulates in vivo. To this end, we first investigated substrate specificity of *ngz_1* and characterized the Michaelis-Menten kinetics for the different identified substrates (Table 2; Supplementary Fig. 9). As expected from our initial, qualitative in vitro characterization, these measurements confirmed the apparent K_M for UNAM to be more than 10-fold smaller than for UNAG or UDP-glucose. Similarly, the determined apparent k_{cat} for UNAM was more than 100-fold higher than for UNAG and UDP-glucose, respectively. This preference became even more prominent when comparing the catalytic efficiency. While this value is rather similar for UNAG and UDP-glucose, it is increased by a factor of approximately 1000 for UNAM, suggesting that UNAM-4P should be the predominant phosphorylated species also in vivo. Thus, we wondered whether UNAG-4P inhibits MurA activity similar as described for UNAG-3P²¹ thereby preventing UNAM synthesis by MurA and MurB. This would lead to accumulating cellular levels of UNAG that can be phosphorylated by *ngz_1*. Hence, we tested any potential inhibition of MurA by UNAG-4P. However, the reaction kinetics of UNAG phosphorylation by MurA remained unaffected when UNAG-4P was added in equimolar amounts to the natural substrate (Fig. 4a). UNAG-4P is rather a dead-end product and cannot be used by MurA anymore. Similarly, MurB activity was also not affected by the presence of any EP-UNAG-4P and it was not reduced to UNAM-4P by the enzyme (Fig. 4a). Importantly, also MurC activity remained the same and the enzyme could not use UNAM-4P as

potential substrate (Fig. 4a). Apparently, none of these enzymes can use their phosphorylated substrates anymore and thus cannot channel any *ngz_1*-phosphorylated peptidoglycan precursor

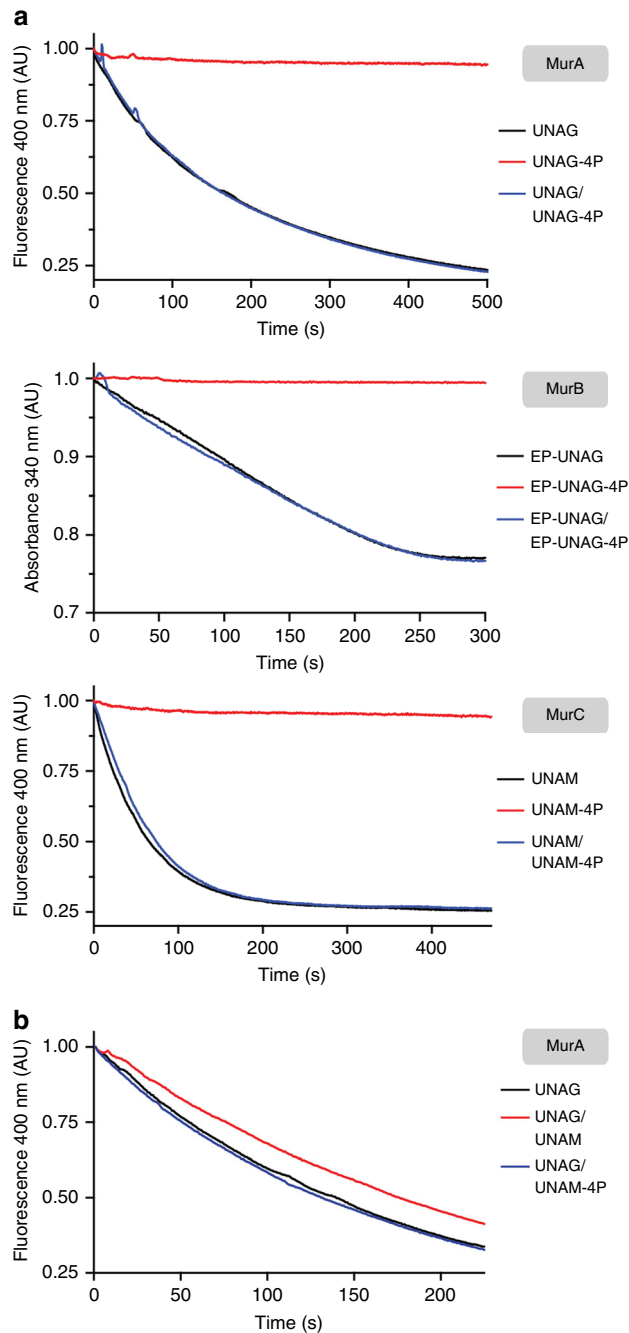


Fig. 4 Effect of *ngz_1* products on enzymes involved in early peptidoglycan synthesis. **a** Effect of in vitro phosphorylated *ngz_1* products on the activity of the first three enzymes of the peptidoglycan synthesis, MurA (monitoring phosphate release), MurB (monitoring NADPH oxidation) and MurC (monitoring phosphate release). In vitro reactions were performed in presence of either the native non-phosphorylated substrate (black; 50 μ M UNAG, 30 μ M EP-UNAG or 50 μ M UNAM), the phosphorylated form (red; 50 μ M UNAG-4P, 30 μ M EP-UNAG-4P, 50 μ M UNAM-4P), or both at equimolar concentrations (blue). Reactions were started upon addition of either 0.25 μ M MurA, 50 nM MurB, or 2 μ M MurC (time 0 s). **b** Effect of UNAM and UNAM-4P on MurA activity. MurA activity assay using 100 μ M UNAG (black) performed in the presence and absence of additional 100 μ M UNAM-4P (blue) or UNAM (red)

Table 2 Michaelis-Menten parameters of *ngz_1* activity

	K_M (mM)	k_{cat} (s^{-1})	k_{cat}/K_M ($mM^{-1}s$)
UNAM _(4 mM ATP)	0.23 ± 0.02	200 ± 7	880
UNAG _(4 mM ATP)	2.8 ± 0.3	1.72 ± 0.05	0.6
UDP-glucose _(4 mM ATP)	6.4 ± 0.7	0.71 ± 0.03	0.1
ATP _(1 mM UNAM)	2.6 ± 0.4	280 ± 16	110
ATP _(20 mM UNAG)	0.34 ± 0.02	1.76 ± 0.02	5.2
ATP _(20 mM UDP-glucose)	0.31 ± 0.05	0.51 ± 0.02	1.7

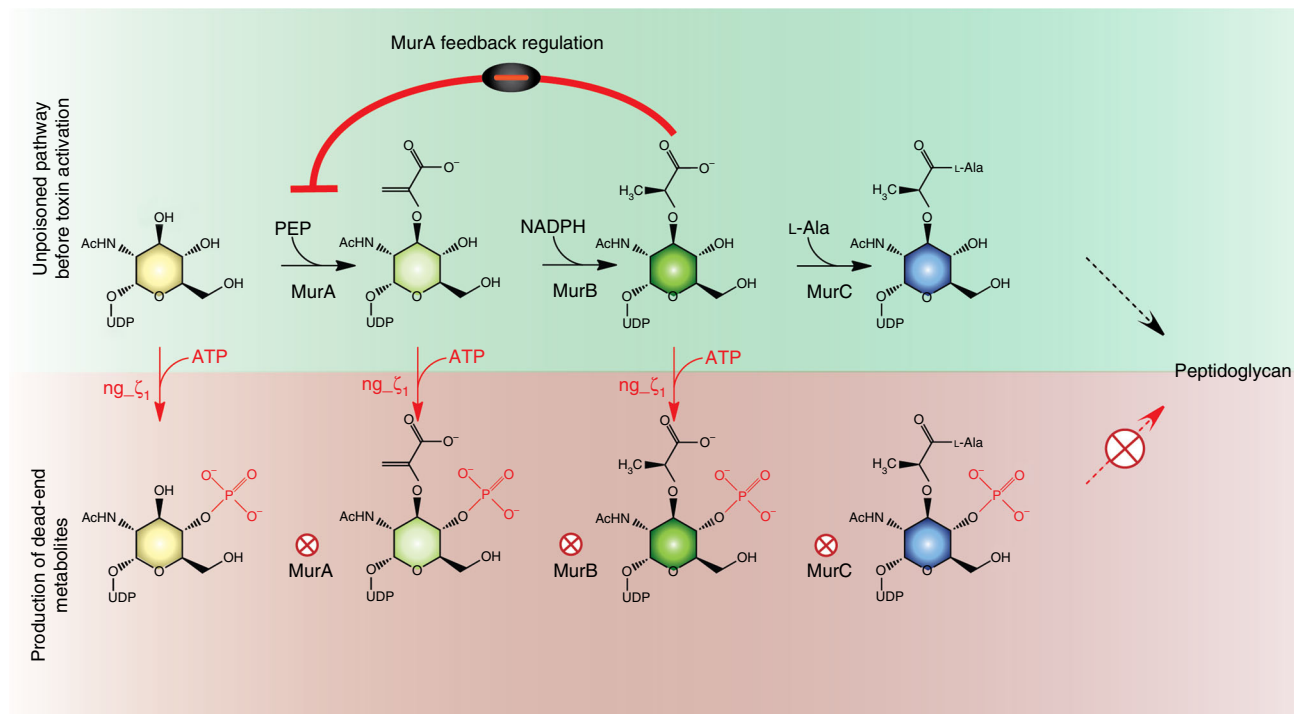


Fig. 5 $ng\zeta_1$ drains precursors from peptidoglycan synthesis at multiple stages. Under normal conditions cytosolic levels of UNAM regulate peptidoglycan synthesis by a negative feedback loop inhibiting MurA. In contrast, once $ng\zeta_1$ becomes active, MurA, MurB, and MurC are depleted from their substrates. All phosphorylated precursors are dead-end metabolites; however, none of them seems to directly inhibit any enzyme of early peptidoglycan synthesis

downstream into the pathway. Ultimately, we also tested whether UNAM-4P can inhibit MurA and thus would still mimic the generic feedback loop in early peptidoglycan synthesis⁴⁰. However, this seems also not to be the case as we could not observe such an inhibition by UNAM-4P (Fig. 4b).

In conclusion, our findings strongly suggest that the cellular substrate concentrations are the key determinants for $ng\zeta_1$ activity. As proof of principle, we tested EP-UNAG, one of the least abundant precursors in cytosolic peptidoglycan synthesis, and observed robust phosphorylation *in vitro* already after 30 min of incubation (Supplementary Fig. 10). Yet, we did not observe EP-UNAG-4P in our small metabolite extracts (Fig. 2a) although the resolution of the HPLC-separation would allow for distinguishing any potentially formed EP-UNAG-4P from all other accumulating species (Supplementary Fig. 11). In conclusion these results strongly suggest that the concentration of the accumulating species is dictated by the cytosolic levels and the toxic phenotype of $ng\zeta_1$ is due to draining all enzymes of early peptidoglycan synthesis from their substrates (Fig. 5).

Discussion

We have studied the gonococcal $ng\zeta_1$ as the paradigm for a hitherto unknown class of abundant zeta kinases that are wired topologically different when compared to previously characterized zeta toxins of Gram-positive bacteria. Thereby, we identified a yet undescribed enzymatic activity. This proteobacterial zeta toxin phosphorylates UDP-activated sugar species at the C4'-OH group of the hexose moiety which eventually causes a lytic phenotype. The toxic activity is inhibited by co-expression of $ng\epsilon_1$ antitoxin, corroborating that the $ng\epsilon_1/ng\zeta_1$ locus encodes for a toxin/antitoxin pair. As expected for a bona-fide type II TA system, we demonstrated protein-protein complex formation between $ng\epsilon_1$ and $ng\zeta_1$, which assemble into a heterodimeric complex.

In contrast to previously studied epsilon antitoxins, the $ng\epsilon_1$ wraps around $ng\zeta_1$ in an extended conformation and does not protrude into the ATP binding site. In this respect, $ng\epsilon_1$ is more similar to the majority of antitoxins of type II TA systems, such as ParD, RelB, MazE and HigA. For these antitoxins an unfolded structure of the unbound protein was either shown or speculated to cause increased proteolytic instability than when complexed with the cognate toxin⁴¹. This intrinsic instability is thought to be important in the regulation of toxin activity in the cell⁴¹. Furthermore, the three-dimensional structure revealed a topological rewiring that seems to distinguish the C4'-OH phosphorylating zeta toxin from the streptococcal C3'-OH phosphorylating zeta subfamily.

Similar to its streptococcal counterparts²¹, $ng\zeta_1$ was shown to phosphorylate peptidoglycan precursors *in vitro* and *in vivo* and cell lysis is a consequence of impairment of peptidoglycan synthesis. However, $ng\zeta_1$ uses a broader substrate spectrum and phosphorylates UNAG as well as UNAM and UDP-glucose at their C4'-OH group. Michaelis-Menten kinetics for the different substrates reveal that $ng\zeta_1$ has highest catalytic efficiency for UNAM. This leads to a significant accumulation of UNAM-4P in the cell, a dead-end metabolite that cannot be modified by MurC. However, contrasting the reduced catalytic efficiency for UNAG *in vitro*, considerable amounts of UNAG-4P were detected *in vivo*. As it is the case for UNAM-4P, also UNAG-4P accumulates as UNAG is also turned into an unsuitable substrate for MurA. In conclusion, both dead-end products of $ng\zeta_1$, UNAG-4P and UNAM-4P, drain MurA and MurC from their substrates (Fig. 5).

We showed that the cellular accumulation of UNAG-4P and UNAM-4P is not due to any inhibition of the Mur enzyme cascade but rather is determined by cellular concentrations of the individual precursors. While UNAM is present at an intracellular concentration of only 30–60 μM in *E. coli*⁴², the concentration of UNAG is approximately ten-fold higher (100–500 μM)^{43–45}.

Therefore UNAG-4P accumulated in vivo although it is only slowly converted by *ng*ζ₁. In fact, EP-UNAG, which we could not detect in vivo as accumulating phosphorylated species but is phosphorylated in vitro by *ng*ζ₁, is less abundant by a factor of 100 compared to UNAG⁴³. Similarly, in vivo accumulation of the even less preferred UDP-glucose is most likely due to its approximately fifty-fold higher concentration (1.5–1.8 mM)⁴⁶. Altogether, formation of these phosphorylated species depletes bacteria from precursors required for de novo synthesis of cell wall components (Fig. 5).

Although our data imply that the drain of the early steps in peptidoglycan synthesis catalysed by MurA, MurB and MurC is very effective, it seems plausible that the addition of a phosphate group to the C4'-OH group will inhibit further downstream processes as well. A non-redundant cascade of enzymes, namely MurC to MurF, subsequently adds an amino acid stem to UNAM, resulting in UNAM-pentapeptide²⁷. *MraY* anchors the UNAM-pentapeptide to cell membrane forming undecaprenyl-pyrophosphoryl-MurNac-pentapeptide, known as lipid I. Finally, lipid I is condensed with the C1'-OH group of UNAG via a β-(1-4)-glycosidic bond by MurG, producing lipid II. This terminates the cytosolic steps of peptidoglycan synthesis as lipid II is flipped either into the periplasmic or extracellular space where transglycosylases catalyze the formation of alternating glycan chain strands. Together with peptide bridges this results in the mesh-like structure of the peptidoglycan layer, which confers rigidity to the cell envelope. Additional inhibitory events are for instance likely at the stage of lipid II formation. MurG which forms the glycosidic bond between a UNAG molecule and lipid I to generate lipid II is highly stereo selective and was shown to exclude the epimer UDP-*N*-acetylgalactosamine, which just differs in the stereochemistry of the C4'-OH⁴⁷. Accordingly, UNAG-4P will most likely also not be accepted by MurG and *ng*ζ₁ therefore will also impair lipid II formation. Although this requires experimental validation, any phosphorylated lipid II would in turn terminate periplasmic glycan strand synthesis by blocking 1–4 glycosidic bond formation of transglycosylases.

Although our study focused on the effect of *ng*ζ₁ on peptidoglycan synthesis, formation of UNAG-4P but also that of UDP-glucose-4P will additionally affect the synthesis of other cell wall components such as lipopolysaccharides (LPS), colanic acids, teichoic acids and the capsule. Similar to its unique role in peptidoglycan synthesis, UNAG is also the central precursor for lipid A (also known as endotoxin) synthesis, the membrane anchor of LPS of Gram-negative bacteria⁴⁸. The highly conserved UDP-*N*-acetylglucosamine acyltransferase *LpxA*, that commits the first step of lipid A synthesis, binds UNAG in a narrow active site⁴⁹, and thus likely will not accept UNAG-4P as substrate, similar as we demonstrated for MurA. While lipid A is highly conserved in Gram-negative bacteria, the composition of the residual LPS is much more diverse and strain specific⁵⁰. Yet, D-glucose is a universally incorporated in many of the latter parts of LPS and thus it is tempting to speculate that formation of UDP-glucose-4P might interfere with their synthesis.

Apparently, zeta toxins encoded by Gram-negative and Gram-positive bacteria do not group into a single uniform kinase family but form at least two functionally and structurally differentiated subfamilies. Although similar in their active site architectures, these toxic enzymes vary in their selectivity and specificity for UDP-activated sugar species, but also in the mechanism by which they interfere with vital cellular processes. On one hand, streptococcal toxins stall the first committed step of peptidoglycan synthesis by inhibition, as formation of UNAG-3P by *PezT* leads to the accumulation of a strong inhibitor of MurA²¹. When a certain level of UNAG-3P is reached the bacterial peptidoglycan synthesis will halt, which can only be relieved by the breakdown

of the inhibitor UNAG-3P. On the other hand, *ng*ζ₁ depletes peptidoglycan and LPS from substrates molecules by forming non-inhibiting, dead-end metabolites and interferes at multiple stages in the pathway. Such a depletion mechanism is in constant competition with the de novo synthesis of cell wall components. This potentially allows a tuning of the peptidoglycan synthesis rates, which gradually decreases with an increase of *ng*ζ₁ activity. It seems plausible, that the different mechanisms reflect an adaptation of the zeta toxins to the peptidoglycan and cell wall structure of bacteria. Whereas the thin periplasmic peptidoglycan mesh in Gram-negative bacteria is very sensitive to changes in its synthesis, the thick outer-membrane peptidoglycan of Gram-positive bacteria may tolerate or even require stronger interference. Zeta toxins might differ in their rates and mechanisms of peptidoglycan synthesis inhibition to still allow recovery once the antitoxin is replenished within a certain frame before cell lysis occurs.

Although experimental evidence has not accumulated for Gram-negative zeta toxins so far, their Gram-positive homologues seem to play a role in bacterial pathogenicity as they have been connected with increased virulence⁵¹, reduced sensitivity to antibiotics and competence^{35,52}, and stable inheritance of mobile genetic elements^{53–55}. It seems plausible that *ng*ζ₁ in Gram-negative bacteria will also have an impact on pathogenicity. *Ng*ζ₁ impairs the synthesis of two essential cell wall components, peptidoglycan and LPS, which are common virulence factors of Gram-negative bacteria. LPS and fragments thereof such as lipid A as well as fragments of peptidoglycan are established immunoactive molecules and the innate immune system of any potential host is specialized in recognizing them. Noteworthy, *N. gonorrhoea* releases a large amount of peptidoglycan fragments such as the Tracheal cytotoxin into the environment⁵⁶, which were shown to be involved in pathogenicity⁵⁷ and by stalling de novo synthesis of peptidoglycan, *ng*ζ₁ will have an impact on that. On the other side, by interfering with lipopolysaccharide synthesis, *ng*ζ₁ potentially may also modulate endotoxin release of pathogenic Gram-negative bacteria and may also be involved in phase variation of the lipopolysaccharide composition to evade the host immune system⁵⁸.

In conclusion, this study showed how a Gram-negative epsilon zeta TA system modifies essential cell wall components and thereby interferes with vital cellular processes. Doubtless, the *nge*_1 / *ng*ζ₁ locus encodes for a plasmid-encoded functional TA system that per se has the potential to support stable plasmid maintenance. However, given that *ng*ζ₁ toxicity interferes with the synthesis of pathogenicity-related cellular compounds at multiple levels, it is tempting to speculate that in addition to its influence on genome plasticity, the *nge*_1/*ng*ζ₁ might modulate Gram-negative bacteria's pathogenicity; a hypothesis which urges for further detailed studies.

Methods

Cloning and protein expression for purification. Cloning of the individual expression constructs was performed according to standard procedures. The sequence of each individual construct was verified by DNA sequencing. A detailed description for the cloning procedure is given in the Supplementary Methods section and in Supplementary Table 2.

For protein purification, individual constructs were transformed into *E. coli* strain BL21(DE3)-RIL cells and bacterial cultures were grown in LB-medium with the appropriate antibiotics to an OD₆₀₀ of 0.5 at 37 °C. Subsequently, the cell cultures were transferred to 20 °C and protein expression was induced by addition of 0.5 mM isopropyl-β-D-thiogalactopyranoside. For production of selenomethionine labeled protein, pET28b_ngo_1/*ng*ζ₁(K115A) transformed cells were grown in an amino acid supplemented minimal medium⁵⁹. Cells were harvested by centrifugation and cell pellets were suspended in their appropriate Ni-NTA equilibration buffers (see Supplementary information). Cell walls were broken by sonication and the supernatant was cleared by centrifugation before loading onto the first column. All proteins used in this study were purified by standard chromatographic procedures which are described in detail in the

Supplementary Information. Protein homogeneity was monitored during all steps by Coomassie stained SDS-PAGE. Protein aliquots were flash-frozen and stored at -80°C .

Phenotype characterization of *nge_1/ngc_1*. Cell lysis accompanied by breakdown of the osmotic barrier was monitored by measuring cell growth at OD_{600} and fluorescence upon propidium iodide (Sigma-Aldrich, St. Louis, USA) influx into *ngc_1* poisoned *E. coli* C41(DE3) cells which are commonly known to tolerate toxin expression much better than BL21(DE3)-RIL. Yet, cells needed to be co-transformed with pET28b_ngo_1 and either pBAD_ngo_1 or pBAD_ngc_1 (K115A), respectively, for stable maintenance of toxic *ngc_1* encoding plasmids. However, promoter leakage was sufficient for stable maintenance during all experiments and *nge_1* remained uninduced during all experiments. Overnight cultures were inoculated in LB-medium containing ampicillin and 0.3% (*w/v*) glucose from single colonies and grown at 37°C . After 1:10 dilution, cell growth was resumed to an OD_{600} of 0.2. Subsequently, this cell culture was diluted with an equal volume of LB medium supplemented with 0.1 mg/ml propidium iodide and 0.2% (*w/v*) L-(+)-arabinose for *ngc_1* or *ngc_1*(K115A) expression. Two hundred microliter of these mixtures were transferred into a 96-well plate (Corning 3651, Corning Inc, Corning, USA) and OD_{600} and propidium iodide fluorescence (excitation: 520 nm, emission: 620 nm) was monitored over 90 min using a Variscan Flash Multimode Reader (Thermo Fisher Scientific, Waltham, USA). Cell cultures for phase contrast and fluorescence microscopy experiments were prepared following the same protocol. Live/dead staining was performed using the LIVE/DEAD BacLight bacterial viability kit (Molecular Probes, Carlsbad, USA).

Analysis of low-molecular-weight metabolite extracts. Low-molecular-weight-metabolite extraction and analysis was performed similarly as previously described²¹. Briefly, *E. coli* C41(DE3) cells harboring pET28b(*nge_1*) and either pBAD_ngo_1 or pBAD_ngc_1(K115A) were grown in 500 ml of LB-medium supplemented with ampicillin to an OD_{600} of 0.3, protein expression was induced upon addition of 0.2% (*w/v*) L-(+)-arabinose and cells were harvested by centrifugation 20 min post-induction. The cell pellets were resuspended in 20 ml ice-cold 80% (*v/v*) aqueous acetonitrile and incubated for 30 min on ice with regular agitation. The supernatant was cleared by centrifugation and the solvent was evaporated. Aliquots were diluted with deionized water, cleared by filtration and adjusted to a common A_{260} of 20 AU. Thirty microliter of sample was applied to a Partisil-5 SAX RACII column (Whatman plc, Maidstone, UK) equilibrated with 5 mM KH_2PO_4 . Bound metabolites were separated in a linear gradient to 500 mM KH_2PO_4 . Fractions containing accumulating UDP-sugars were pooled, bound to a MonoQ 5/50 GL column equilibrated with deionized water and eluted in a linear gradient to 1 M ammonium acetate pH 8.0 (32 column volumes (CV)). Solvent and volatile compounds were removed by repeated evaporation and purified compounds were dissolved in deionized water, analyzed with a Bruker maXis II mass spectrometer (Bruker Corporation, Billerica, USA) and fragmented by collision-induced dissociation.

Oligomeric state determination of the *nge_1/ngc_1* complex. The oligomeric state of the *nge_1/ngc_1* protein complex was determined by multi-angle light scattering (Wyatt, Santa Barbara, USA) coupled to size-exclusion chromatography using a Superdex200 10/300 GL column (GE Healthcare, 50 mM MES-NaOH pH 6.0 and 200 mM NaCl). Forty microliter of either *nge_1/ngc_1* protein complex or protein standard mixture (Bio-Rad, Hercules, USA) were injected and the recorded data were analyzed using the ASTRA software (Wyatt).

Synthesis and purification of UDP-sugars. UNAM was prepared through successive enzymatic conversion of UNAG by MurA and MurB. To avoid potential inhibition of MurA by UNAM⁴⁰, 300 μM UNAG was first converted to EP-UNAG by MurA. Therefore, 1 μM MurA was mixed with 1 mM phosphoenolpyruvate (PEP) and 400 μM NADPH in a buffer composed of 50 mM Tris-HCl, pH 8.0, 50 mM NaCl and 10 mM KCl. After 3 h incubation at room temperature, 0.5 μM MurB were added and the reaction was further incubated overnight. The reaction mixture was diluted in deionized water (1:2), loaded onto a MonoQ 10/100 GL column equilibrated with deionized water. Bound residual UNAG and NADP were removed by washing the column with 300 mM ammonium acetate pH 8.0 and UNAM was eluted with 350 mM of ammonium acetate pH 8.0. Fractions containing UNAM were pooled and concentrated by evaporation. Finally, UNAM was desalted by size exclusion chromatography using a Superdex75 10/300 GL column equilibrated with deionized water. UNAM containing fractions were pooled and concentrated by evaporation.

Synthesis of EP-UNAG was performed similar to the production of UNAM but neither MurB nor NADPH was included in the reaction mixture. The reaction was incubated for 2.5 h at room temperature and EP-UNAG was purified by anion exchange and size exclusion chromatography as described for UNAM.

For production of UNAM-4P, 300 μM UNAM was incubated with 10 nM *ngc_1* in preparation buffer (50 mM MES-NaOH pH 6.0, 200 mM NaCl, 0.5 mM EDTA, 14 mM KCl and 2 mM PEP) supplemented with 4 mM MgCl_2 and 1 mM ATP. For recycling of ATP from ADP, 7.2 U of pyruvate kinase (PK)/10.8 U of lactate dehydrogenase (LDH) were included in the reaction. After incubation at 25°C for

6 h, the reaction mixture was diluted in deionized water and loaded onto a MonoQ 5/50 GL column equilibrated with deionized water. Bound ATP was eluted by washing the column with 30 mM MgCl_2 . Subsequently, the column was washed in four steps with water, 1 mM EDTA pH 8.0, water and 170 mM ammonium bicarbonate, pH 8.0. Pure UNAM-4P was eluted with 1 M ammonium bicarbonate, pH 8.0. Concentrating and desalting of UNAM-4P was performed similar as described for UNAM and EP-UNAG.

The enzymatic conversion of 250 μM EP-UNAG to EP-UNAG-4P by *ngc_1* (1 μM) was performed in preparation buffer supplemented with 1 mM MgCl_2 , 0.5 mM ATP and 0.6 U PK/0.9 U LDH. Phosphorylated EP-UNAG was loaded onto a Mono Q 5/50 GL column equilibrated with water and eluted in a gradient of 60 CV to 1 M ammonium acetate pH 8.0. Fractions containing EP-UNAG-4P were pooled and concentrated by evaporation. For quantitative removal of ammonium acetate, the pellet of EP-UNAG-4P was re-dissolved in pure water and re-concentrated twice. The correct identity for the different UDP-activated sugar species was verified by ESI-MS and the final concentration of was determined spectroscopically ($\epsilon_{260} = 10.100 \text{ cm}^{-1} \text{ M}^{-1}$)^{60,61}.

Chromatographic *ngc_1* phosphorylation assays. Substrate phosphorylation by *ngc_1* was analyzed using a chromatographic assay. Two hundred and fifty micromolar EP-UNAG, UDP-glucose or UNAG and 0.5 mM ATP were mixed in reaction buffer B (50 mM MES pH 6.0, 200 mM NaCl, 1 mM MgCl_2 , 14 mM KCl, 2 mM PEP, 0.6 U PK and 0.9 U LDH) in a total volume of 180 μl . Reactions were started by addition of 1 μM *ngc_1* and incubated at 25°C for different time points (5 min, 3, 12, and 24 h). A reaction lacking *ngc_1* was used as a control. The progression of the reaction was followed via anion exchange chromatography. The mixture was applied to MonoQ 5/50 GL column equilibrated with deionized water. After an initial isocratic elution with 200 mM ammonium acetate pH 8.0, a linear gradient to 1 M ammonium acetate was performed (33 CV for UDP-glucose and UNAG, 60 CV for EP-UNAG). The specific retention volume and characteristic 260:280 ratio were used to identify the nucleotide species.

NMR characterization of UNAG-4P. UNAG-4P was dissolved in 99.9% D_2O at a concentration of 6 mg/ml and spectra were recorded at 25°C using a Varian 500 NMR system spectrometer (Agilent). NMR experiments were processed and analyzed using the MestReNova 10.0 (Mestrelab Research) software. Atom names and assignment is given in Supplementary Fig. 5.

Signal assignment of ^1H NMR experiments (500 MHz, ^1H -H-COSY, D_2O): $\delta = 7.98$ (d, 1H, $^3J_{\text{HH}} = 8.2$ Hz, H-U6), 6.0–5.98 (m, 2H, H-U5, H-1'), 5.53 (dd, 1H, $^3J_{\text{HH}} = 7.3$ Hz, $^3J_{\text{HP}} = 3.2$ Hz, H-1), 4.40–4.37 (m, 2H, H-2', H-3'), 4.30 (m, 1H, H-4'), 4.28–4.25 (m, 1H, H-5'a), 4.22–4.18 (m, 1H, H-5'b), 4.08–3.97 (m, 4H, H-2, H-3, H-4, H-5), 3.90–3.84 (m, 2H, H-6a, H-6b), 2.09 (s, 3H, H-8) ppm.

Assignment of ^{13}C NMR experiments (152.7 MHz, APT, HSQC, D_2O): $\delta = 174.63$ (C, C=O), 166.14 (C, C=O), 151.72 (C, C=O), 141.55 (CH, C-U6), 102.59 (CH, C-U5), 94.03 (CH, $J_{\text{CP}} = 6.2$ Hz, C-1), 88.38 (CH, C-1'), 83.16 (CH, $J_{\text{CP}} = 9.0$ Hz, C-4'), 73.71 (CH, C-3'), 73.25 (CH, $J_{\text{CP}} = 4.7$ Hz, C-5), 72.03 (CH, $J_{\text{CP}} = 5.7$ Hz, C-4), 70.41 (CH, C-3), 69.57 (CH, C-2'), 64.90 (CH_2 , $J_{\text{CP}} = 6.2$ Hz, C-5'), 60.11 (CH_2 , C-6), 53.35 (CH, $J_{\text{CP}} = 8.5$ Hz, C-2), 22.00 (CH_3 , C-8) ppm.

Assignment of ^{31}P NMR decoupling experiments (202.4 MHz, D_2O): $\delta = 0.91$ (s, P-4), -11.46 (d, $J_{\text{PP}} = 19.7$ Hz, P-5'), -13.16 (d, $J_{\text{PP}} = 20.0$ Hz, P-1) ppm.

Structure determination. Crystals of wild type *nge_1/ngc_1* or selenomethionine labelled *nge_1/ngc_1*(K115A) protein complex were grown at a concentration of 22 mg/ml using a sitting drop vapor diffusion setup. Best crystals grew as stacked plates using a reservoir solution of 100 mM sodium citrate pH 4.5 and 1.8 M $(\text{NH}_4)_2\text{SO}_4$. Crystals were transferred to a solution containing 100 mM sodium citrate pH 4.5, 2 M $(\text{NH}_4)_2\text{SO}_4$ and 20% (*v/v*) propylene glycol and flash cooled in liquid nitrogen. UNAM or UNAM-4P at a concentration of 20 mM were added to the cryo-protectant and incubated for 10 min during soaking experiments.

Se-SAD and native diffraction data were collected at the Swiss Light Source X10SA beamline and processed with the XDS software package⁶², 5% of the reflection were randomly selected for calculation of R_{free} and inherited to all datasets. Initial phases were obtained using the SHELXC and SHELXD⁶³ from Se-SAD on *nge_1/ngc_1*(K115A) protein complex crystals. Phases from the Se-substructure obtained from SHELXD were improved using Phaser⁶⁴, Parrot⁶⁵ and DM⁶⁶. An initial model was built using Coot⁶⁷ and refined using the simulated annealing protocol of CNS⁶⁸. Subsequently, the model was improved in iterative cycles of manual building in Coot and refinement using Refmac⁶⁹. Final structure validation was performed using MolProbity⁷⁰. Figures were prepared using PYMOL⁷¹.

***ngc_1* kinase activity assays.** Phosphorylation of different UDP-activated sugar species by *ngc_1* was monitored using a coupled spectroscopic assay in which formation of ADP is coupled to consumption of NADH⁷². Conversion of NADH to NAD^+ was monitored spectroscopically at 340 nm (Jasco V650, Jasco, Mary's Court, USA). All reactions were performed in assay buffer (50 mM MES-NaOH pH 6.0, 200 mM NaCl, 1 mM EDTA, 6 mM MgCl_2 , 14 mM KCl, 1 mM PEP, 0.25 mM NADH, 1 mg/ml BSA, 0.6 U PK and 0.9 U LDH) in a total volume of 100 μl , unless otherwise explicitly stated.

In qualitative experiments, where the apparent velocities of different UDP-activated sugars were compared, 10 nM of ng ζ _1 and 4 mM Mg $^{2+}$ -ATP were added to the assay buffer and incubated until a stable baseline was observed. The reaction was started upon addition of either 50 μ M of UNAG, UNAM, or UDP-glucose.

For the titration experiments aiming at determination of the Michaelis Menten parameters for UDP-sugar species, 4 mM Mg $^{2+}$ -ATP and 200 nM (in case of UNAG and UDP-glucose) or 5 nM (in case of UNAM) ng ζ _1 were added to the assay buffer. Reactions were started by addition of varying concentrations of different substrates (UNAG: 0.31–40 mM, UDP-glucose: 0.31–20 mM, UNAM: 23–750 μ M). For UNAM titration the amount of PK and LDH was increased threefold. While a stable baseline was observed when using a low enzyme concentration (5 nM ng ζ _1), at 200 nM ng ζ _1 a weak basal ATPase background activity was observed. This apparent basal reaction velocity was determined to be in the range of 0.03–0.13 s $^{-1}$ and was subtracted for baseline correction in these experiments. In experiments aiming at determination of the Michaelis Menten parameters for ATP, 200 nM (in case of UNAG or UDP-glucose) or 10 nM (in case of UNAM) ng ζ _1 and varying concentrations of Mg $^{2+}$ -ATP from 31.25 μ M–4 mM were added to the reaction mixture and incubated until a stable baseline was reached. In case of a weak basal ATPase activity a baseline correction was performed as described above. The reaction was started by addition of either 20 mM UNAG or UDP-glucose or 1 mM UNAM.

The apparent initial velocities for each measurement were determined by the Spectra Manager Analysis software (JASCO), converted to apparent k_{cat} and each measurement was fitted to the Michaelis Menten equation with GraphPad Prism v.5 (GraphPad, La Jolla, USA).

Activity of peptidoglycan synthesis enzymes. MurA and MurC activities were monitored in an assay that couples the release of inorganic phosphate to the cleavage of fluorescent 7-methylguanosine 73 by purine nucleoside phosphorylase (PNPase, Sigma-Aldrich, St. Louis, USA). The resulting decrease in fluorescence at 400 nm (bandwidth 5 nm) was measured with a spectrofluorometer (FP-8500, JASCO) using 300 nm as the excitation wavelength (bandwidth 5 nm). MurA reactions were performed in a total volume of 400 μ l in a buffer containing 50 mM Hepes-NaOH pH 7.5, 50 mM NaCl, 1 mM PEP, 0.5 mM EDTA, 50 μ M 7-methylguanosine and 0.3 U PNPase supplemented with either 50 μ M UNAG, 50 μ M UNAM or both (50 μ M each). After a stable baseline was reached the reaction was started upon addition of 0.25 μ M MurA. A potential inhibitory effect of UNAM and UNAM-4P on the MurA activity was tested through the addition of 100 μ M UNAM or UNAM-4P to a reaction containing 100 μ M UNAG as substrate.

Similarly, MurC activity was measured in a total volume of 400 μ l in a buffer containing 50 mM Hepes-NaOH pH 7.5, 0.1 mM EDTA, 10 mM MgCl $_2$, 300 μ M Mg $^{2+}$ -ATP, 0.5 mM L-Ala, 0.3 U PNPase, 50 μ M 7-methylguanosine, and either 50 μ M UNAM, 50 μ M UNAM-4P or both. After reaching a stable baseline 2 μ M MurC were added to start the reaction.

MurB activity was followed spectroscopically by directly monitoring the oxidation of NADPH at 340 nm in buffer containing 50 mM Tris-HCl pH 8.0, 50 mM KCl, and 150 μ M NADPH in a total volume of 100 μ l. Subsequently, either 30 μ M EPUNAG, 30 μ M EPUNAG-4P or both (30 μ M each) were added to the reaction which was started upon addition of 50 nM MurB.

Data availability. Coordinates and structure factor amplitudes have been deposited in the Protein Data Bank under accession codes 6EPG, 6EPH and 6EPI. Other data are available from the corresponding author upon reasonable request.

Received: 1 October 2017 Accepted: 2 March 2018

Published online: 27 April 2018

References

- Leplae, R. et al. Diversity of bacterial type II toxin-antitoxin systems: a comprehensive search and functional analysis of novel families. *Nucleic Acids Res* **39**, 5513–5525 (2011).
- Pandey, D. P. & Gerdes, K. Toxin-antitoxin loci are highly abundant in free-living but lost from host-associated prokaryotes. *Nucleic Acids Res.* **33**, 966–976 (2005).
- Yamaguchi, Y., Park, J. H. & Inouye, M. Toxin-antitoxin systems in bacteria and archaea. *Annu Rev. Genet* **45**, 61–79 (2011).
- Gerdes, K., Christensen, S. K. & Lobner-Olesen, A. Prokaryotic toxin-antitoxin stress response loci. *Nat. Rev. Microbiol* **3**, 371–382 (2005).
- Lobato-Marquez, D., Diaz-Orejas, R. & Garcia-Del Portillo, F. Toxin-antitoxins and bacterial virulence. *FEMS Microbiol Rev.* **40**, 592–609 (2016).
- Wang, X. & Wood, T. K. Toxin-antitoxin systems influence biofilm and persister cell formation and the general stress response. *Appl. Environ. Microbiol* **77**, 5577–5583 (2011).
- Haurlyuk, V., Atkinson, G. C., Murakami, K. S., Tenson, T. & Gerdes, K. Recent functional insights into the role of (p)ppGpp in bacterial physiology. *Nat. Rev. Microbiol* **13**, 298–309 (2015).
- Schuster, C. F. & Bertram, R. Toxin-antitoxin systems are ubiquitous and versatile modulators of prokaryotic cell fate. *FEMS Microbiol Lett.* **340**, 73–85 (2013).
- Gerdes, K. & Maisonneuve, E. Bacterial persistence and toxin-antitoxin loci. *Annu Rev. Microbiol* **66**, 103–123 (2012).
- Goeders, N. & Van Melderen, L. Toxin-antitoxin systems as multilevel interaction systems. *Toxins (Basel)* **6**, 304–324 (2014).
- Pedersen, K. et al. The bacterial toxin RelE displays codon-specific cleavage of mRNAs in the ribosomal A site. *Cell* **112**, 131–140 (2003).
- Zhang, Y. et al. MazF cleaves cellular mRNAs specifically at ACA to block protein synthesis in *Escherichia coli*. *Mol. Cell* **12**, 913–923 (2003).
- Cook, G. M. et al. Ribonucleases in bacterial toxin-antitoxin systems. *Biochim Biophys. Acta* **1829**, 523–531 (2013).
- Germain, E., Castro-Roa, D., Zenkin, N. & Gerdes, K. Molecular mechanism of bacterial persistence by HipA. *Mol. Cell* **52**, 248–254 (2013).
- Kaspy, I. et al. HipA-mediated antibiotic persistence via phosphorylation of the glutamyl-tRNA-synthetase. *Nat. Commun.* **4**, 3001 (2013).
- Castro-Roa, D. et al. The Fic protein Doc uses an inverted substrate to phosphorylate and inactivate EF-Tu. *Nat. Chem. Biol.* **9**, 811–817 (2013).
- Ogura, T. & Hiraga, S. Mini-F plasmid genes that couple host cell division to plasmid proliferation. *Proc. Natl Acad. Sci. USA* **80**, 4784–4788 (1983).
- Bernard, P. et al. The F plasmid CcdB protein induces efficient ATP-dependent DNA cleavage by gyrase. *J. Mol. Biol.* **234**, 534–541 (1993).
- Gerdes, K. et al. Mechanism of postsegregational killing by the hok gene product of the parB system of plasmid R1 and its homology with the relF gene product of the *E. coli* relB operon. *EMBO J.* **5**, 2023–2029 (1986).
- Brantl, S. Bacterial type I toxin-antitoxin systems. *RNA Biol.* **9**, 1488–1490 (2012).
- Mutschler, H., Gebhardt, M., Shoeman, R. L. & Meinhart, A. A novel mechanism of programmed cell death in bacteria by toxin-antitoxin systems corrupts peptidoglycan synthesis. *PLoS Biol.* **9**, e1001033 (2011).
- Mutschler, H. & Meinhart, A. epsilon/zeta systems: their role in resistance, virulence, and their potential for antibiotic development. *J. Mol. Med.* **89**, 1183–1194 (2011).
- Ceglowski, P., Boitsov, A., Chai, S. & Alonso, J. C. Analysis of the stabilization system of pSM19035-derived plasmid pBT233 in *Bacillus subtilis*. *Gene* **136**, 1–12 (1993).
- Khoo, S. K. et al. Molecular and structural characterization of the PezAT chromosomal toxin-antitoxin system of the human pathogen *Streptococcus pneumoniae*. *J. Biol. Chem.* **282**, 19606–19618 (2007).
- Meinhart, A., Alonso, J. C., Strater, N. & Saenger, W. Crystal structure of the plasmid maintenance system epsilon/zeta: functional mechanism of toxin zeta and inactivation by epsilon 2 zeta 2 complex formation. *Proc. Natl Acad. Sci. USA* **100**, 1661–1666 (2003).
- Saraste, M., Sibbald, P. R. & Wittinghofer, A. The P-loop—a common motif in ATP- and GTP-binding proteins. *Trends Biochem Sci.* **15**, 430–434 (1990).
- Barreteau, H. et al. Cytoplasmic steps of peptidoglycan biosynthesis. *FEMS Microbiol. Rev.* **32**, 168–207 (2008).
- Han, Q. et al. Crystal structure of *Xanthomonas* AvrRxo1-ORF1, a type III effector with a polynucleotide kinase domain, and its interactor AvrRxo1-ORF2. *Structure* **23**, 1900–1909 (2015).
- Triplett, L. R. et al. AvrRxo1 is a bifunctional type III secreted effector and toxin-antitoxin system component with homologs in diverse environmental contexts. *PLoS One* **11**, e0158856 (2016).
- Schuebel, F. et al. 3'-NADP and 3'-NAADP, two metabolites formed by the bacterial type III effector AvrRxo1. *J. Biol. Chem.* **291**, 22868–22880 (2016).
- Shidore, T. et al. The effector AvrRxo1 phosphorylates NAD in planta. *PLoS Pathog.* **13**, e1006442 (2017).
- Rocker, A. & Meinhart, A. A cis-acting antitoxin domain within the chromosomal toxin-antitoxin module EzeT of *Escherichia coli* quenches toxin activity. *Mol. Microbiol.* **97**, 589–604 (2015).
- Pachulek, E. & van der Does, C. Conjugative plasmids of *Neisseria gonorrhoeae*. *PLoS One* **5**, e9962 (2010).
- Morse, S. A., Johnson, S. R., Biddle, J. W. & Roberts, M. C. High-level tetracycline resistance in *Neisseria gonorrhoeae* is result of acquisition of streptococcal tetM determinant. *Antimicrob. Agents Chemother.* **30**, 664–670 (1986).
- Tabone, M., Ayora, S. & Alonso, J. C. Toxin zeta reversible induces dormancy and reduces the UDP-N-acetylglucosamine pool as one of the protective responses to cope with stress. *Toxins* **6**, 2787–2803 (2014).
- Kwon, S. K., Kim, S. K., Lee, D. H. & Kim, J. F. Comparative genomics and experimental evolution of *Escherichia coli* BL21(DE3) strains reveal the landscape of toxicity escape from membrane protein overproduction. *Sci. Rep.* **5**, 16076 (2015).
- Studier, F. W., Daegelen, P., Lenski, R. E., Maslov, S. & Kim, J. F. Understanding the differences between genome sequences of *Escherichia coli*

- B strains REL606 and BL21(DE3) and comparison of the *E. coli* B and K-12 genomes. *J. Mol. Biol.* **394**, 653–680 (2009).
38. Barupal, D. K., Lee, S. J., Karoly, E. D. & Adhya, S. Inactivation of metabolic genes causes short- and long-range dys-regulation in *Escherichia coli* metabolic network. *PLoS One* **8**, e78360 (2013).
 39. Holm, L., Kaariainen, S., Rosenstrom, P. & Schenkel, A. Searching protein structure databases with DALI Lite v.3. *Bioinformatics* **24**, 2780–2781 (2008).
 40. Mizyed, S., Oddone, A., Byczynski, B., Hughes, D. W. & Berti, P. J. UDP-N-acetylmuramic acid (UDP-MurNAc) is a potent inhibitor of MurA (enolpyruvyl-UDP-GlcNAc synthase). *Biochemistry* **44**, 4011–4017 (2005).
 41. Brzozowska, I. & Zielenkiewicz, U. Regulation of toxin-antitoxin systems by proteolysis. *Plasmid* **70**, 33–41 (2013).
 42. Mengin-Lecreulx, D., Flouret, B. & van Heijenoort, J. Cytoplasmic steps of peptidoglycan synthesis in *Escherichia coli*. *J. Bacteriol.* **151**, 1109–1117 (1982).
 43. Mengin-Lecreulx, D., Flouret, B. & van Heijenoort, J. Pool levels of UDP N-acetylglucosamine and UDP N-acetylglucosamine-enolpyruvate in *Escherichia coli* and correlation with peptidoglycan synthesis. *J. Bacteriol.* **154**, 1284–1290 (1983).
 44. Mengin-Lecreulx, D., Siegel, E. & van Heijenoort, J. Variations in UDP-N-acetylglucosamine and UDP-N-acetylmuramyl-pentapeptide pools in *Escherichia coli* after inhibition of protein synthesis. *J. Bacteriol.* **171**, 3282–3287 (1989).
 45. Namboori, S. C. & Graham, D. E. Enzymatic analysis of uridine diphosphate N-acetyl-D-glucosamine. *Anal. Biochem.* **381**, 94–100 (2008).
 46. Buckstein, M. H., He, J. & Rubin, H. Characterization of nucleotide pools as a function of physiological state in *Escherichia coli*. *J. Bacteriol.* **190**, 718–726 (2008).
 47. Ha, S. et al. The kinetic characterization of *Escherichia coli* MurG using synthetic substrate analogues. *J. Am. Chem. Soc.* **121**, 8415–8426 (1999).
 48. Raetz, C. R. et al. Discovery of new biosynthetic pathways: the lipid A story. *J. Lipid Res* **50**, S103–S108 (2009).
 49. Ulaganathan, V., Buetow, L. & Hunter, W. N. Nucleotide substrate recognition by UDP-N-acetylglucosamine acyltransferase (LpxA) in the first step of lipid A biosynthesis. *J. Mol. Biol.* **369**, 305–312 (2007).
 50. Wang, X. & Quinn, P. J. Lipopolysaccharide: biosynthetic pathway and structure modification. *Prog. Lipid Res* **49**, 97–107 (2010).
 51. Harvey, R. M. et al. A variable region within the genome of *Streptococcus pneumoniae* contributes to strain-strain variation in virulence. *PLoS One* **6**, e19650 (2011).
 52. Chan, W. T. & Espinosa, M. The *Streptococcus pneumoniae* pezAT toxin-antitoxin system reduces beta-lactam resistance and genetic competence. *Front. Microbiol.* **7**, 1322 (2016).
 53. Yao, X. et al. The chromosomal SezAT toxin-antitoxin system promotes the maintenance of the SsPI-1 pathogenicity island in epidemic *Streptococcus suis*. *Mol. Microbiol.* **98**, 243–257 (2015).
 54. Zielenkiewicz, U. & Ceglowski, P. The toxin-antitoxin system of the streptococcal plasmid pSM19035. *J. Bacteriol.* **187**, 6094–6105 (2005).
 55. Ceglowski, P., Boitsov, A., Karamyan, N., Chai, S. & Alonso, J. C. Characterization of the effectors required for stable inheritance of *Streptococcus pyogenes* pSM19035-derived plasmids in *Bacillus subtilis*. *Mol. Gen. Genet* **241**, 579–585 (1993).
 56. Rosenthal, R. S. Release of soluble peptidoglycan from growing gonococci: hexaminidase and amidase activities. *Infect. Immun.* **24**, 869–878 (1979).
 57. Melly, M. A., McGee, Z. A. & Rosenthal, R. S. Ability of monomeric peptidoglycan fragments from *Neisseria gonorrhoeae* to damage human fallopian-tube mucosa. *J. Infect. Dis.* **149**, 378–386 (1984).
 58. van der Woude, M. W. & Baumler, A. J. Phase and antigenic variation in bacteria. *Clin. Microbiol. Rev.* **17**, 581–611 (2004).
 59. Van Duyne, G. D., Standaert, R. F., Karplus, P. A., Schreiber, S. L. & Clardy, J. Atomic structures of the human immunophilin FKBP-12 complexes with FK506 and rapamycin. *J. Mol. Biol.* **229**, 105–124 (1993).
 60. Voet, D., Gratzner, W. B., Cox, R. A. & Doty, P. Absorption spectra of nucleotides, polynucleotides, and nucleic acids in the far ultraviolet. *Biopolymers* **1**, 193–208 (1963).
 61. Dawson, R. M. C. *Data for Biochemical Research* (Clarendon Press, Oxford, 1986).
 62. Kabsch, W. Automatic processing of rotation diffraction data from crystals of initially unknown symmetry and cell constants. *J. Appl. Cryst.* **26**, 795–800 (1993).
 63. Sheldrick, G. M. A short history of SHELX. *Acta Crystallogr A* **64**, 112–122 (2008).
 64. McCoy, A. J. et al. Phaser crystallographic software. *J. Appl. Cryst.* **40**, 458–674 (2007).
 65. Cowtan, K. Recent developments in classical density modification. *Acta Crystallogr D Biol. Crystallogr* **66**, 470–478 (2010).
 66. Cowtan, K. dm: An automated procedure for phase improvement by density modification. *Jt. CCP4 ESF-EACBM News. Protein Crystallogr.* **31**, 34–38 (1994).
 67. Emsley, P. & Cowtan, K. Coot: model-building tools for molecular graphics. *Acta Cryst.* **D60**, 2126–2132 (2004).
 68. Brunger, A. T. Version 1.2 of the crystallography and NMR system. *Nat. Protoc.* **2**, 2728–2733 (2007).
 69. Murshudov, G. N., Vagin, A. A. & Dodson, E. J. Refinement of macromolecular structures by the maximum-likelihood method. *Acta Cryst.* **D53**, 240–255 (1997).
 70. Chen, V. B. et al. MolProbity: all-atom structure validation for macromolecular crystallography. *Acta Crystallogr D Biol. Crystallogr* **66**, 12–21 (2010).
 71. DeLano, W. L. The PyMOL Molecular Graphics System. (DeLano Scientific, Palo Alto, CA, USA, 2002).
 72. Berghauer, J. A reactive arginine in adenylate kinase. *Biochim Biophys. Acta* **397**, 370–376 (1975).
 73. Kulikowska, E., Bzowska, A., Wierchowski, J. & Shugar, D. Properties of two unusual, and fluorescent, substrates of purine-nucleoside phosphorylase: 7-methylguanosine and 7-methylinosine. *Biochim Biophys. Acta* **874**, 355–363 (1986).

Acknowledgements

We thank C. van der Does (University Freiburg, Germany) for providing plasmid DNA and are grateful to T. Barends, J. Reinstein, and T. Clausen for helpful discussions. We acknowledge C. Roome for support of the crystallographic software and IT, F. Jungblut for technical assistance and the PXII staff for their support in setting up the beamline. Diffraction data were collected at the Swiss Light Source, beamline X10SA, Paul Scherrer Institute, Villigen, Switzerland. We are grateful to I. Schlichting for continuous encouragement and support. This work was financially supported by the Max Planck Society. A. M. is supported by the Chica and Heinz Schaller Foundation, Heidelberg, Germany.

Author contributions

A.R. and M.P. designed and performed most of the experiments and wrote the manuscript. T.K. performed some of the kinetic experiments and nucleotide activated sugar purifications and wrote the manuscript. R.S. purified and crystallized the protein complex. C.B. performed NMR and analyzed the data. A.M. performed together with A.R. the crystallographic experiments, was involved in experimental design and wrote the manuscript.

Additional information

Supplementary Information accompanies this paper at <https://doi.org/10.1038/s41467-018-03652-8>.

Competing interests: The authors declare no competing interests.

Reprints and permission information is available online at <http://npng.nature.com/reprintsandpermissions/>

Publisher's note: Springer Nature remains neutral with regard to jurisdictional claims in published maps and institutional affiliations.



Open Access This article is licensed under a Creative Commons Attribution 4.0 International License, which permits use, sharing, adaptation, distribution and reproduction in any medium or format, as long as you give appropriate credit to the original author(s) and the source, provide a link to the Creative Commons license, and indicate if changes were made. The images or other third party material in this article are included in the article's Creative Commons license, unless indicated otherwise in a credit line to the material. If material is not included in the article's Creative Commons license and your intended use is not permitted by statutory regulation or exceeds the permitted use, you will need to obtain permission directly from the copyright holder. To view a copy of this license, visit <http://creativecommons.org/licenses/by/4.0/>.

© The Author(s) 2018